PNAS RESEARCH ARTICLE | PHYSICS

Unconventional magnetic oscillations in a kagome Mott insulator

Guoxin Zheng[a,1], Yuan Zhu[a,1], Kuan-Wen Chen[a,1], Byungmin Kang[b], Dechen Zhang[a], Kaila Jenkins[a], Aaron Chan[a], Zhenyuan Zeng[c,d], Aini Xu[c,d], Oscar A. Valenzuela[e], Joanna Blawat[e], John Singleton[e], Shiliang Li[c,d,f], Patrick A. Lee[b,2], and Lu Li[a,2]

Affiliations are included on p. 8.

Contributed by Patrick A. Lee; received October 16, 2024; accepted December 27, 2024; reviewed by Young S. Lee and Michael R. Norman

In metals, electrons in a magnetic field undergo cyclotron motion, leading to oscillations in physical properties called quantum oscillations. This phenomenon has never been seen in a robust insulator because there are no mobile electrons. We report an exception to this rule. We study a Mott insulator on a kagome lattice which does not order magnetically down to milli-Kelvin temperatures despite antiferromagnetic interactions. We observe a plateau at magnetization equal to $\frac{1}{9}$ Bohr magneton per magnetic ion, accompanied by oscillations in the magnetic torque, reminiscent of quantum oscillations in metals. The temperature dependence obeys Fermi distribution. These phenomena are consistent with a quantum spin liquid state whose excitations are fermionic spinons with a Dirac-like spectrum coupled to an emergent gauge field.

quantum spin liquid | magnetization plateau | quantum oscillations

In conventional metals, electrons form Landau Levels in a magnetic field, leading to magnetic oscillations in their physical properties. In the absence of charged Fermi surfaces, a robust insulator is NOT expected to host any quantum oscillations. Therefore, the recent observations of Landau Level quantization in narrow-gap, correlated Kondo insulators (1–6) have created a lot of excitement. These developments lead naturally to the next question: Can quantum oscillations be observed in wide-gap correlated insulators, in particular, in nonmagnetic Mott insulators? In lattices with an odd number of electrons per unit cell, strong repulsion between electrons may result in a Mott insulator, where the electrons are localized on lattice sites, forming $S = \frac{1}{2}$ moments. The moments interact via antiferromagnetic (AF) interactions, and usually form an ordered AF state. In frustrated lattices, magnetic ordering may be suppressed due to frustration and quantum fluctuations, resulting in a novel state of matter called the quantum spin liquid (7, 8). Some versions of the quantum spin liquid are predicted to host exotic particles such as gapless fermions which carry $S=\frac{1}{2}$ but no charge (called spinons), coupled to an emergent gauge field (9, 10). Indeed it has been proposed that these low energy excitations can lead to quantum oscillations in certain spin liquid candidates which are charge insulators (11).

The kagome lattice exhibits a high degree of frustration and is a strong candidate for hosting a spin liquid (9, 10, 12–14). Experimentally, herbertsmithite is the most famous example of a kagome Mott insulator, leading to fascinating discoveries (15). Unfortunately, while the Cu ions in the kagome layers remain pristine (16, 17), a significant fraction of the Zn sites that lies between the kagome planes are substituted by Cu, creating impurity spins that can dominate the low temperature spectrum, thermodynamics, and magnetic properties (18, 19). A search for oscillations in this kagome Mott insulator was conducted but was unsuccessful (20). The recent discovery of $YCu_3(OH)_6Br_2[Br_{1-y}(OH)_y]$ (YCOB), in which Zn is replaced by Y, solves the site mixing problem thanks to the very different ionic sizes of Y and Cu (21–24). These materials do not show magnetic order down to 50 mK, but there remains disorder in the exchange constants caused by the random replacement of Br above and below the Cu hexagons by OH (23). It should also be mentioned that the so-called perfect Y-based kagome crystal $YCu_3(OH)_6Cl_3$ with Cl instead of Br and without the OH disorder, was the first to be developed (25) and later found to order at 15 K (26). This is not unexpected because the presence of a Dzyaloshinskii Moriya (DM) coupling is theoretically known to favor ordering (27–29). On the other hand, the closely related Y-kapellasite $Y_3Cu_9(OH)_{19}Cl_8$ has a tripled inplane unit cell and orders at a lower temperature of 2.1 K (30). Therefore, OH substitution and the subsequent disorder may play a role in suppression AF ordering, as discussed in a recent detailed study (31). The role of disorder is a complicated question and we will defer further comments to

Significance

Fractionalization is a central theme of modern condensed matter physics, as exemplified by the fractional quantum Hall effect. Another example that has been long sought after is quantum spin liquid, where antiferromagnetic order has been suppressed by quantum fluctuations and the spin–charge separation of electrons can lead to charge-neutral spinons. Applying ultrasensitive magnetometry to a kagome-lattice Mott insulator with a 3-eV charge gap, we report quantum oscillations in the magnetic torque. The observation is strong evidence for fermionic spinons, and an effective gauge field which allows the coupling of the applied magnetic field to charge-neutral particles. A phenomenological model of spinon band structure that includes Dirac nodes near the 1/9 magnetization plateau shows predictions consistent with the observed oscillation patterns.

Author contributions: P.A.L. and L.L. designed research; G.Z., Y.Z., K.-W.C., B.K., D.Z., K.J., A.C., Z.Z., A.X., O.A.V., J.B., J.S., S.L., P.A.L., and L.L. performed research; G.Z. and L.L. analyzed data; and G.Z., P.A.L., and L.L. wrote the paper.

Reviewers: Y.S.L., Stanford University; and M.R.N., Argonne National Laboratory.

The authors declare no competing interest.

[1] G.Z., Y.Z., and K.-W.C. contributed equally to this work.

[2] To whom correspondence may be addressed. Email: palee@mit.edu or luli@umich.edu.

This article contains supporting information online at https://www.pnas.org/lookup/suppl/doi:10.1073/pnas.2421390122/-/DCSupplemental.

Discussion below. At this point, we simply note this class of crystals exhibits a great deal of richness and complexity and we are motivated to study the magnetic behavior of YCOB under intense magnetic fields. We should also emphasize that while YCOB in zero field has been claimed to harbor Dirac spinons (22, 23) and have been under intense studies (31, 32), the current paper focuses on the behavior under strong magnetic field, and the connection of the state of matter that we uncover with the zero field case is left for future studies.

Results

Five YCOB single-crystal samples are used in the torque magnetometry measurements, and two batches of YCOB single crystals are measured using extraction magnetometry. Fig. 1*A* shows the crystal structure of YCOB, with detailed information given in ref. 22. Samples M1 and M2 comprise several thin crystals stacked in a Vespel ampoule with their *c*-axes or *ab*-planes aligned. We use compensated-coil extraction magnetometry (33) (see sketch in *SI Appendix*, Fig. S2*A*) to measure the overall magnetization in pulsed magnetic fields $\mu_0 H$ of up to 60 T and 73 T. The field is applied parallel and perpendicular to crystal *c*-axis in separate experiments. Sample S1 is the main single crystal measured using cantilever magnetometry in a DC magnet ($0 \leq \mu_0 H \leq 41$ T). The magnetic torque of three more YCOB single crystals (Sample S2, D1, and D2) was measured in two DC magnets, and the torque of one more YCOB single crystal (Sample S5) was measured in a 60 T pulsed magnet. Details and sample growth information can be found in *Materials and Methods*.

The overall magnetization curves shown in the *Upper* panel of Fig. 1*B* are derived by averaging data from multiple field pulses recorded with $T \approx 0.6$ K. A small anisotropy is observed in both M and the characteristic fields; the ratio is consistent with the reported g-factor anisotropy (22). For $\mu_0 H > 55$ T, the magnetization reaches a plateau at around $0.35\mu_B$ per Cu atom (where μ_B is the Bohr magneton), indicating the $\frac{1}{3}$ plateau (34–38). According to the model in ref. 36, the $\frac{1}{3}$ plateau begins at $0.83J$ in a kagome Heisenberg antiferromagnet, where J is the nearest-neighbor AF exchange constant. We can therefore estimate that $J \approx 44.5$ K, which is comparable to the value reported in ref. 23. In addition to the $\frac{1}{3}$ plateau, at $\mu_0 H \approx 18$ T, a feature appears in the $M(H)$ curve, with $M \approx 0.11\mu_B$ per Cu, providing evidence for a $\frac{1}{9}$ plateau. Studies conducted in parallel to ours have also reported this plateau (39, 40). Note that the $\frac{1}{9}$ plateau has been anticipated by theory. Density-matrix renormalization group (DMRG) work on the Heisenberg model on the kagome lattice has revealed a $\frac{1}{9}$ plateau (36), considered to be an indication of exotic physics (36, 38, 41) while tensor network methods favor a valence bond solid which triples the unit cell (42, 43). A recent variational Monte Carlo calculation based on the Gutzwiller projection of a fermionic state yields a Z3 spin liquid with energy in good agreement with the DMRG calculation (44).

Further information comes from the differential magnetic susceptibility $\chi \equiv \frac{dM}{dH}$ shown in the *Lower* panel of Fig. 1*B*; a V-shape dip appears at the center of the $\frac{1}{9}$ plateau. The dips are centered at $\mu_0 H_0 \approx 20.4$ T for $H \parallel c$ and $\mu_0 H_0 \approx 22.3$ T for $H \perp c$. These field differences are consistent with the g-factor anisotropy. Another batch of single crystals were prepared as Sample M2 for extraction magnetometry to get a more detailed T-dependence of the magnetization. The corresponding magnetic susceptibility is shown in Fig. 1*C*, and the raw magnetization data are given in *SI Appendix*, Fig. S2*A*. We notice that the minimum in magnetic susceptibility around $H_0 \sim 20$ T does not saturate when T approaches zero, even at the lowest temperature (0.6 K$\sim$ 0.01J). To quantitatively evaluate the temperature dependence of the $\frac{1}{9}$ plateau, the value

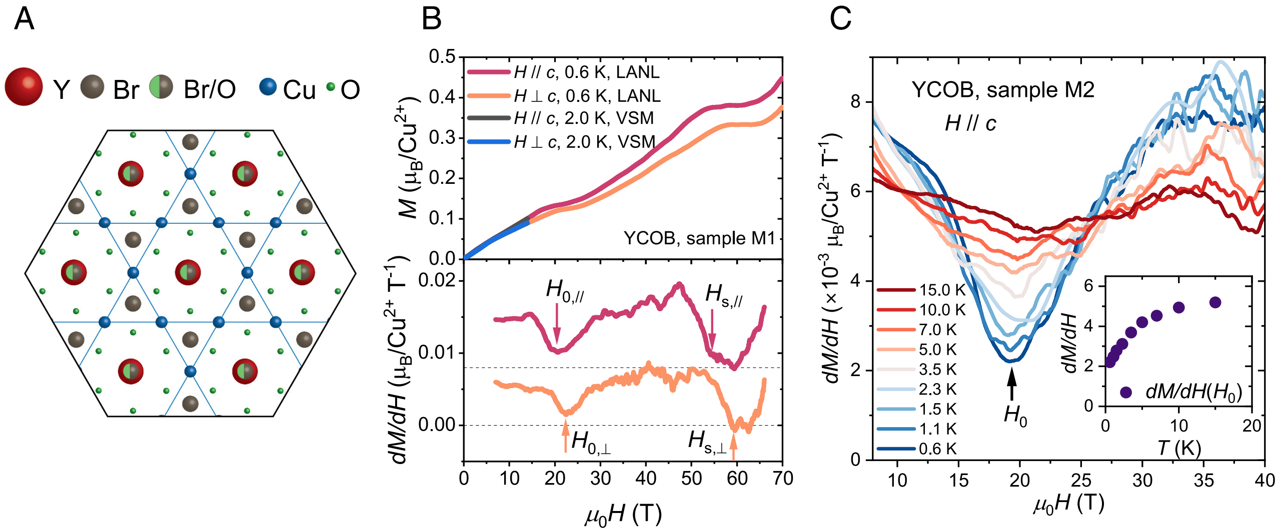

Fig. 1. Magnetization plateaus. (*A*) Structure of YCOB. Cu and Y are in the $z = 0$ plane. The Br sites above and below Y are randomly admixed with OH. The O sites around the hexagon are alternately buckled up and down off the plane. (*B*) *Top* panel: Magnetization M of YCOB sample measured in pulsed magnetic fields of up to 70 T with $\mathbf{H} \parallel c$ and $\mathbf{H} \perp c$. The measurement setup is shown in the *Inset* of *SI Appendix*, Fig. S2*A*. Both $\frac{1}{9}$ and $\frac{1}{3}$ plateaus were observed in M. Black and blue curves show measurements in the PPMS up to 14 T in the two directions for comparison. *Bottom* panel: The differential magnetic susceptibility $\frac{dM}{dH}$ measured in pulsed fields. The low-field arrow indicates the location of the Dirac point crossing H_0, and the high-field arrow indicates the onset of the $\frac{1}{3}$ plateau H_S. H_0 and H_S along the ab-plane shift to higher fields, consistent with the known g-factor anisotropy. For clarity, the $H \parallel c$ curve is shifted with zero marked by the dotted line. (*C*) The temperature dependence of $\frac{dM}{dH}$ measured on YCOB sample M2 with $H \parallel c$. *Inset*: The temperature dependence of $\frac{dM}{dH}$ at $H = H_0$, which corresponds to the minimum within the $\frac{1}{9}$ plateau region. The unit of $\frac{dM}{dH}$ is $10^{-3}\mu_B/\mathrm{Cu}^{2+}/\mathrm{T}$.

of $\frac{\mathrm{d}M}{\mathrm{d}H}$ at $H = H_0$ is plotted against T in the *Inset* of Fig. 1*C*, showing a quasi-linear behavior as $T \to 0$, contrasting sharply with the fully gapped behavior observed at the $\frac{1}{3}$ plateau in other antiferromagnetic systems which can be understood in terms of magnon excitations (45, 46). The potential origin of this unconventional $\frac{1}{9}$ plateau will be explained in *Discussion*.

The torque magnetometry results confirm the $\frac{1}{9}$ plateau and reveal more detail due to the finer resolution. As shown in the *Inset* of Fig. 2*A*, the torque magnetometry setup measures the torque due to the crystal in the direction perpendicular to the $M - H$ plane as $\tau = \mu_0 V \mathbf{M} \times \mathbf{H} = \mu_0 V M_t H$, with V the sample volume and M_t the magnetization component perpendicular to H. In other words, instead of detecting the overall magnetization, torque magnetometry picks up the anisotropic response, either due to a higher order H-dependence of M or off-diagonal terms of the magnetic susceptibility tensor. The angular dependence of τ measured in YCOB sample S1 is shown in Fig. 2*A*, where θ is the angle between $\vec{H}$ and $\hat{c}$. First, the bump observed in the $M - H$ curve of Sample M1 and M2 at $\mu_0 H \approx 18$ T also occurs in τ. More surprisingly, a series of dips and peaks are observed at $H > 20$ T, which are clearly seen in the derivative of torque across most angles, as shown in Fig. 2*B*. Taking second derivatives of τ Fig. 2*C* with respect to H effectively removes any quadratic background, allowing the oscillatory pattern to be further clarified without creating new oscillations.

To further investigate these unusual oscillations, the T-dependence of τ, the resulting M_t, the first derivate of torque $\frac{\mathrm{d}\tau}{\mathrm{d}H}$ at $\theta = -32.6°$ are plotted in Fig. 3*A*. Similar data for two other values of θ are plotted in *SI Appendix*, Fig. S6. The magnetic oscillations above 20 T are rapidly suppressed with increasing temperature, becoming unobservable above 3 K. In Fig. 3*B*, the second derivative of the torque is plotted to offer a clearer representation of the magnetic oscillations. The oscillations are approximately evenly spaced in H, in contrast to the $1/H$ periodicity of magnetic quantum oscillations in metals. As can be seen in Fig. 3*B*, as T increases, the oscillation amplitude shrinks while the period stays the same. Fig. 3*C* shows the average amplitude of the $\frac{\mathrm{d}\tau}{\mathrm{d}H}$ oscillations, after background subtraction in the range [24 T, 35.7 T], obtained using Fast Fourier Transformation (FFT—see *SI Appendix*, section S5), and plotted as a function of temperature T. The result can be fitted with the Lifshitz–Kosevich (LK) formula, which gives the T-dependence of amplitudes, i.e., $\delta M \propto \frac{aT}{\sinh(aT)}$, for quantum oscillations due to fermions with mass m^* (47). Using $a = \frac{2\pi^2}{e\hbar} \frac{m^*}{\mu_0 H \cos(\theta)}$, the resulting $m^*/m_e = 4$ is similar to the values $m^*/m_e = 5.2$ found for another angle (*SI Appendix*, Fig. S6). Although the data points in Fig. 3*C* can also be fitted with other forms, such as a Gaussian distribution, we opted for the LK fit because it is based on known physics and produces a mass that is consistent with that extracted from an entirely different measurement based on the Dirac spinon model discussed later.

To confirm the observation of the oscillations, 4 additional YCOB crystals were measured in 3 different high-field magnets, with H up to 41 or 45 T in DC magnetic fields and up to 60 T in a pulsed magnet. *SI Appendix*, Table S1 summarizes the limits of the samples we tested and whether the observation was confirmed. *SI Appendix*, section S6 and Fig. S10 present a direct comparison of the torque signals. Additionally, we conducted a control experiment by intentionally doping Cl at the Br site (31). The control sample retains the same structure and the kagome lattice formed by Cu, yet shows neither the $\frac{1}{9}$ plateau nor the magnetic oscillations (*SI Appendix*, Fig. S9).

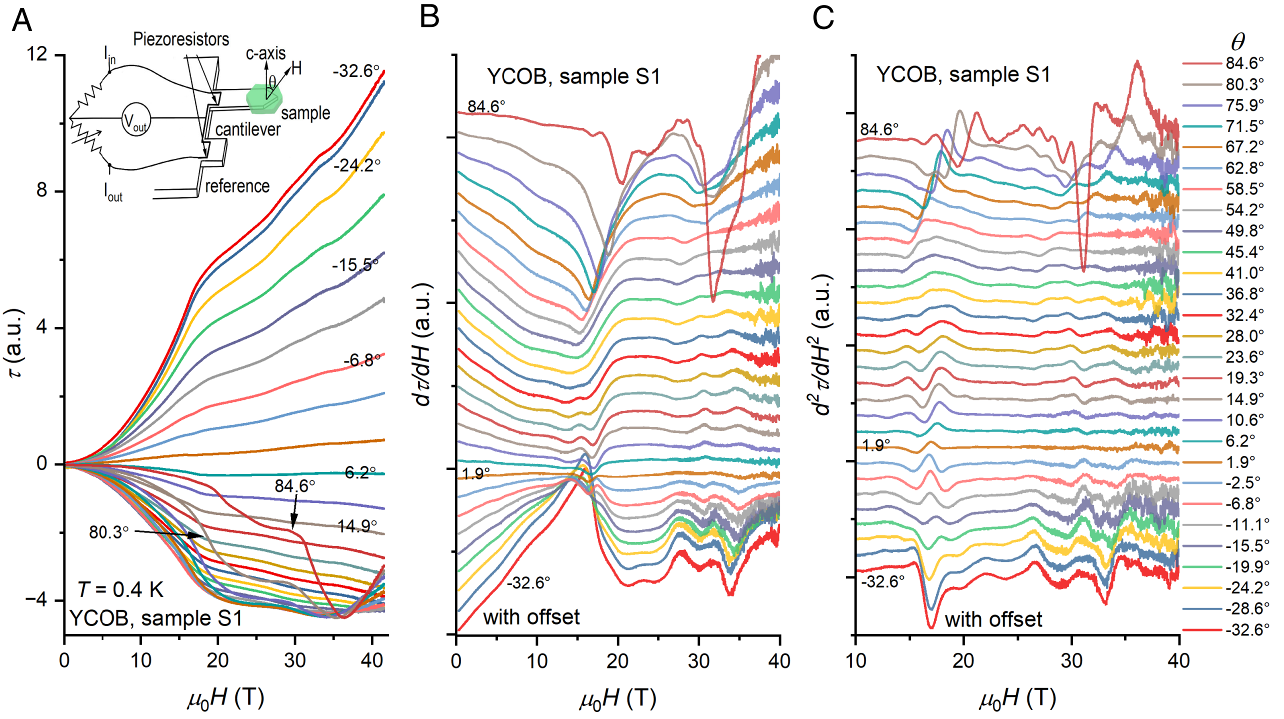

Fig. 2. Oscillations in magnetic torque. (*A*) Raw magnetic torque τ data, (*B*) $\mathrm{d}\tau/\mathrm{d}H$, and (*C*) $\mathrm{d}\tau^2/\mathrm{d}H^2$ versus magnetic field H at $T = 0.4$ K at different angles of YCOB sample S1, measured with a piezo-resistive cantilever. θ is defined by the angle between $\vec{H}$ and $\hat{c}$. The magnetic torque was measured using a piezoresistive cantilever [setup shown in the (*A*) *Inset*] in a resistive magnet up to 41 T.

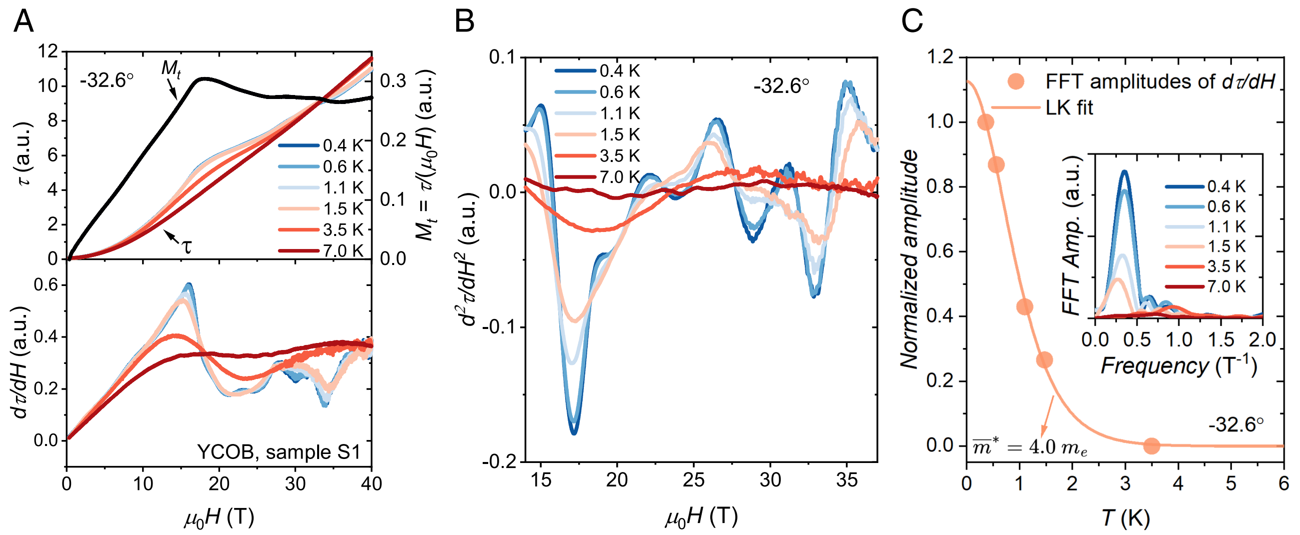

Fig. 3. Temperature dependence of the magnetic oscillations. (*A*) Temperature dependence of magnetic torque τ (*Top* panel, *Left*), $\mathrm{d}\tau/\mathrm{d}H$ (*Bottom* panel), and (*B*) $\mathrm{d}^2\tau/\mathrm{d}H^2$ of YCOB sample S1 as a function of applied magnetic field up to 41 T at $\theta = -32.6°$. The transverse magnetization $M_t = \tau/\mu_0 H$ at $T = 0.4$ K is shown in the *Top* panel of (*A*) to compare with the magnetization data. Oscillations are observed in magnetic field above the $\frac{1}{9}$ plateau at $B_0 \approx 20$ T. The amplitude of the oscillation smears out as the temperature rises. (*C*) The normalized FFT amplitude of the $\mathrm{d}\tau/\mathrm{d}H$ oscillatory patterns after background subtraction (*SI Appendix*, Fig. S5*B*). The background subtraction method is shown in *SI Appendix*, Fig. S5*A*. The solid curve shows the LK fitting, and the fitted average effective mass $\bar{m}^*$ is 4 m_e. *Inset*: The FFT analysis (*SI Appendix*, section S5) within FFT window [24 T, 35.7 T].

Discussion

We first summarize the experimental observations. The measurements of magnetization and magnetic torque both reveal the $\frac{1}{9}$ plateau in H along both c-axis and the ab-plane. The magnetic torque measurement further reveals many oscillations above the $\frac{1}{9}$ field, whose positions are aligned consistently in the first derivative $\frac{\mathrm{d}\tau}{\mathrm{d}H}$ and the second derivative $\frac{\mathrm{d}^2\tau}{\mathrm{d}H^2}$. These oscillations are roughly evenly spaced in H. Furthermore, the oscillation positions shift systematically as the H-field is rotated from the c-axis to the ab-plane. As T increases, the oscillation positions stay the same, and their amplitude shrinks. These observations call for interpretation.

We begin with a discussion of the 1/9 plateau. The $\frac{\mathrm{d}M}{\mathrm{d}H}$ curve shown in Fig. 1*C* is V-shaped and shows a linear T dependence at the dip down to our lowest temperature of 0.4 K. This suggests that gapless excitations exist at the plateau. In contrast, the 1/9 plateau reported in ref 40 is found to saturate at low temperature and has been interpreted as forming a spin gap below 1.6 K. Two possible gapped scenarios, a Z3 spin liquid state (36) and valence bond crystal (42, 43) have been proposed to explain the emergent gap. Possible explanations for these differing observations may include sample variations, as discussed in detail in ref. 31, and the temperature resolution of the magnetization measurements performed in the high field. Further experiments are needed to clarify this discrepancy.

Next, to understand the origin of magnetic oscillations, we need to rule out extrinsic effects such as metallic impurity islands inside this 3-eV gapped insulating sample. As shown in *SI Appendix*, Figs. S8 and S10, five different samples grown in separate batches have been measured in two DC magnets and one pulsed magnet to confirm the reproducibility of the observations. Additionally, an impurity metallic phase would produce $1/H$ periodic magnetic oscillations, a common feature in metals, which is contrary to the quasi-H-periodic oscillation pattern shown in Fig. 3*B*.

Therefore, an explanation that is intrinsic to the system is needed. In the following, we review examples in the literature where structures as a function of magnetic field have been seen in magnetization data and interpreted as a series of phase transitions. We will see that these data and their interpretation are quite different from our data in their temperature and angle dependences. Next, we will discuss an interpretation based on the Dirac spinon model. We will show that a version of this model produces a simple formula (Eqs. **3** and **4**) which accounts for the complex temperature and angle dependence with a set of internally consistent parameters. Of course, this does not constitute proof, but at the very least, the model allows us to organize the data in a systematic way.

Magnetic Phase Transitions. We note that recently oscillatory behavior in the thermal conductivity has been reported in the spin liquid candidate α-RuCl$_3$ and interpreted as quantum oscillations (48). This interpretation has been challenged and alternative proposals involving a series of magnetic phase transitions have been made (49–51). We would like to point out that there is an important difference between these oscillations and our observations. In α−RuCl$_3$ the oscillations depend on the components of the magnetic field that are in-plane, whereas our observations are sensitive to the out-of-plane field as in conventional quantum oscillations while showing additional complex variations with the tilt angle from the c-axis. Nevertheless, this debate inspired us to consider an alternative explanation based on assuming a series of magnetic transitions. Indeed, some kagome magnet systems are known to exhibit multiple plateau transitions, as observed in kagome insulators (37, 52) and kagome metals (53). In these materials, the lattice might be weakly distorted by the Zeeman energy of the magnetic field, leading to different superlattice phases of spins and resulting in classical spin up-up-down (UUD) plateaus. Experimentally, these plateaus are directly revealed in the overall magnetization. As T increases, these plateau transition fields usually shift, reflecting the delicate balance between the lattice distortion and thermal activation (53). Similarly, triangular lattice quantum magnet insulators may exhibit a dominant UUD plateau, with additional states emerging in different fields (45, 54). These plateau states are generally observed through magnetization measurements. Torque measurements on these quantum magnets (55, 56) resolve the transition fields marking the beginning and end of these plateau states. The angular dependence typically does not show significant shifts in the transition field due to the isotropic nature of the Zeeman energy, with any shifts arising from the weak anisotropy of the g-factor. On the other hand, the peaks generally shift with increasing temperature, and sometimes neighboring peaks merge (55).

Therefore, the first possible scenario is that our observed magnetic oscillations originate from multiple plateau states, similar to those seen in other kagome magnets. In this case, one would associate each oscillation peak (or valley) with a phase transition. We would expect sharp features in the $\frac{\mathrm{dM}}{\mathrm{dH}}$ as one crosses a phase boundary, as is seen in Cs_2CuCl_4 (57), or a more "rounded" transition feature in $\frac{\mathrm{dM}}{\mathrm{dH}}$, as in Cs_2CuBr_4 (58). Our data do not show these spikes and remain sinusoidal down to the lowest temperature. Our peak positions do not show any T dependence as seen in the experiments on other systems. Furthermore, since ordered phases live between the phase boundaries, one expects to observe typical phase transition signatures in the magnetization as the temperature reaches the critical temperature, with power law exponents. This is seen in Cs_2CuCl_4 (57). We do not see any evidence of such phase transitions. However, it should be noted that the possibility that the sharp features are broadened by disorder in the exchange constant which is intrinsic to YCOB (23) cannot be fully ruled out.

Finally, an important shortcoming of this scenario is that it fails to explain the systematic angular dependence of the many observed oscillations. One would need to make ad hoc assumptions about how the phase boundaries shift with the magnetic field.

Dirac Spinon Model. Below we describe a phenomenological fermionic model, sketched in Fig. 4, which can explain the $\frac{1}{9}$ magnetization plateau, and its temperature dependence, plus features of the magnetization oscillations and their temperature dependence that we have identified so far.

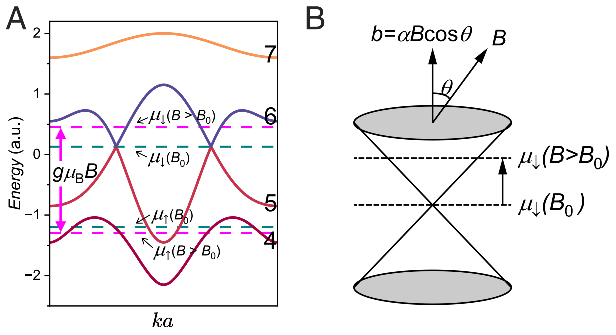

Fig. 4. Dirac spinon model. (*A*) A schematic band structure for bands 4 to 7 out of 9 bands taken along a line in k space that cuts through a Dirac node between bands 5 and 6. The chemical potentials of up and down spin near the $\frac{1}{9}$ plateau are also plotted, showing the pinning of the up spin chemical potential for $B > B_0$. (*B*) The sketch of one Dirac node around B_0.After applying the magnetic field, the chemical potential μ of one spin will shift upward due to the Zeeman effect. The gauge field of the spinors seen is $b = \alpha B\cos\theta$, where α is a coupling constant.

As phenomenology, we do not attempt to start with a microscopic model, but it should be mentioned that YCOB is believed to have substantial randomness in the exchange coupling which is related to the random replacement of one of the Br sites off the kagome plane by OH (23). This replacement distorts the Cu–OH–Cu bonds, leading to an alternation of the exchange J around the hexagon. This bond alternation is ordered in Y-kapellasite (30), leading to a tripling of the inplane unit cell and a large reduction in the ordering temperature. In YCOB these distorted hexagons are randomly distributed and depending on their fraction (31) can totally suppress AF order. It appears that this kind of correlated disorder plays an important role in countering the DM term and stabilizing a spin liquid ground state for zero or small magnetic fields. The precise magnitude and the effect of this correlated disorder is not well known. In ref. 23 a variation of J by as much as 70% has been proposed. However, this number is based on fitting a hump in the magnetic susceptibility data, and its reliability is in question because it was shown in ref. 31 that the hump is insensitive to the fraction of hexagons and may have a different origin. We note that neutron scattering at $B = 0$ found peaks which are narrow in momentum space that disperse rapidly (32), which suggests that randomness may not be playing a dominant role. Furthermore, in the presence of a large magnetic field near the 1/9 plateau, the Zeeman energy is large and the effect of disorder may be less important. Within our picture, randomness can lead to a broadening of the fermion bands. Given the level of uncertainty, we do not take disorder broadening into account in our phenomenological model.

We begin by addressing the V-shaped χ and its T dependence as shown in Fig. 1*C*. In the case of the $\frac{1}{3}$ magnetization plateau, a V-shaped χ has previously been proposed to be indicative of an incompletely developed plateau (59), but our temperature dependence in Fig. 1*C* does not support this interpretation because in that case χ typically saturates at low temperatures. This is in contrast with the approximate linear T behavior at the dip minimum seen in Fig. 1 *C*, *Inset*. (See *SI Appendix*, Fig. S2 for a more detailed comparison.) The V-shaped χ and the gapless behavior motivate us to consider a fermionic model. In a model where the low energy excitations are fermions occupying energy bands, χ is proportional to the fermion density of states $D(E)$ at the Fermi level. Consequently, the V-shaped $\chi \propto |B - B_0|$ and its linear T dependence shown in Fig. 1 *C*, *Inset* suggests that $D(E) \propto |E|$. (Since χ is small, $B \approx \mu_0 H$; we define $B_0 = \mu_0 H_0$ and will use B and $\mu_0 H$ interchangeably.) This suggests the V-shape could originate from Dirac fermions. Furthermore, the temperature dependence of χ can be fitted by a Fermi–Dirac based thermal broadening model, as shown in *SI Appendix*, section S1 and Figs. S2*B* and S4, which is another evidence for the fermionic picture.

Regardless of their origin, if the excitations are fermionic, what must the band structure look like? In order to explain the $\frac{1}{9}$ plateau, there must be a gap or a Dirac node in the fermion band so that the down (up) spin bands hold 5 (4) fermions. This requires 9 bands, which can come only from a tripling of the unit cell. This is accomplished either by breaking translation symmetry, or (without doing that) by imposing $2\pi/3$ flux per unit cell. We note that the Gutzwiller projection of the latter state is precisely the Z3 spin liquid state found in ref. 44. In either case, we sketch the schematic band structure of the fourth to sixth bands in Fig. 4*A* (For simplicity, we assume the band dispersion is the same for up and down spin. Since the result depends only on the density of states near the Fermi levels, the result remains the same if the bands are spin-dependent.) A V-shaped χ suggests a linear density of states. In order to explain the V-shaped χ, we assume a Dirac node with velocity v_D between bands 5 and 6. A small gap at the Dirac node will not change our analysis. Bands 4 and 5 may be separated by a gap or may overlap. We assume the latter for reasons that will become clear later.

At field $B = B_0$, the down spin chemical potential $\mu_\downarrow$ is at the Dirac point while the up spin chemical potential $\mu_\uparrow$ is between bands 4 and 5, as shown in Fig. 4*A*. Upon increasing $B > B_0$, $\mu_\downarrow$ moves up while $\mu_\uparrow$ moves down, and their difference is given by the Zeeman splitting $g\mu_B B$. The differential susceptibility $\chi = \frac{\mathrm{d}M}{\mathrm{d}H}$ is given by (*SI Appendix*, section S1 and Eq. **S11**)

$$\chi \propto ((D(\mu_\uparrow)^{-1} + D(\mu_\downarrow))^{-1})^{-1}, \qquad \textbf{[1]}$$

where $D(E)$ is the density of states at energy E. Note that instead of adding the density of states at the up and down spin chemical potentials, we add their inverse. Hence, χ is dominated by the smaller of the two. To understand this rather counterintuitive result, let us consider the situation shown in Fig. 4*A* where $\mu_\downarrow$ is near the Dirac node and has a much smaller density of states compared with $\mu_\uparrow$ which lies in the middle of bands 4 and 5. In order to fix the total fermion density, $\mu_\uparrow$ will be nearly pinned while $\mu_\downarrow$ moves up at the rate of the full Zeeman splitting $g\mu_B B$. The differential susceptibility $\mathrm{d}M/\mathrm{d}H$ then comes mainly from the movement of $\mu_\downarrow$ and is sensitive to $D(\mu_\downarrow)$, in agreement with Eq. **1**. We parameterize this movement by $\mu_\downarrow = (g'/2)\mu_B$, where $g' \approx 2g$. It is satisfying that the doubling of the g-factor that was needed to fit the thermal smearing of the V-shaped χ comes out naturally, as discussed in *SI Appendix*, section S1. If there were a gap between bands 4 and 5, χ would remain zero as long as $\mu_\uparrow$ is in this gap, giving rise to a U-shaped χ, which does not agree with the data.

The above discussion shows that the susceptibility data alone already place considerable constraints on the nature of the fermion bands. Can the same band structure explain the quantum oscillations? Owing to the large charge gap, the fermions must be charge neutral, leading us to interpret the fermions as fractionalized spinons that are necessarily coupled to an emergent gauge field (9, 10). Recall that conventional two-dimensional (2D) metals exhibit magnetization oscillation due to Landau quantization:

$$M(B) \propto -\sin\left(\frac{A_{FS}\phi_0}{2\pi B\cos(\theta)} - \varphi\right), \qquad \textbf{[2]}$$

where A_{FS} is the Fermi surface area and $\phi_0 = h/e$.

The application of this equation to our problem requires several modifications. First, for $B > B_0$ a Fermi surface is formed in the down spin band with an area $A_{FS} = \pi k_F^2$, where $k_F = \frac{g'\mu_B}{2\hbar v_D}(B - B_0)$. Second, spinons with a Fermi surface are coupled to a U(1) gauge field, which is the 2D analog of the electromagnetic field in our world (9–11). Because it is 2D, the gauge magnetic field b is always perpendicular to the plane and produces Landau levels in the spinon spectrum. It is useful to introduce the parameter $\alpha = b/(B\cos(\theta))$ to characterize the relative strength of the gauge field and B. Then we can simply replace B in the denominator of Eq. **2** by $|\alpha|B$. The origin of b and its relation to the external field B will be discussed later.

Putting everything together, for $kT << \mu_\downarrow$ the oscillatory part of the torque per area L^2 is given by (*SI Appendix*, section S3)

$$\frac{\tau}{BL^2} = -\sin\theta C_0(B - B_0)\frac{aT}{\sinh aT}\sin(2\pi\frac{(B-B_0)^2}{B\cdot\Delta B} - \varphi), \qquad \textbf{[3]}$$

where $C_0 = |\alpha|\frac{e}{\pi^2\hbar}g'\mu_B$ and

$$\Delta B = 2e\hbar\frac{|\alpha|v_D^2}{((g'/2)\mu_B)^2}\cos\theta. \qquad \textbf{[4]}$$

It is important to note that B plays a dual role. Due to the Zeeman effect, it gives rise to a Fermi surface for the down spin band, leading to the $(B - B_0)^2$ factor inside the sine in Eq. **3**. This B dependence is isotropic apart from the small g factor anisotropy. On the other hand, B also produces a finite gauge field b, which depends on the component of the B-field perpendicular to the plane. This gives rise to quite complex behavior as a function of B-field and its angle θ. As we will see, a single equation (Eq. **3**) captures the complexity of the data as well as their temperature dependence.

Next, we compare the experimental results with predictions from the Dirac spinon model. Fig. 5*A* presents the θ−dependence of the magnetic oscillations, and the background subtraction method is given in *SI Appendix*, Fig. S5*A*. The roughly even spacing of the magnetic oscillations persists over a wide range of θ. Moreover, as θ changes, the oscillation peaks and dips gradually shift, and the intervals between them progressively decrease. This suggests an orbital origin of the oscillations. Together with the Lifshitz–Kosevich temperature dependence, we are led to attempt a Landau Level indexing as a function of B based on Eq. **3** (See *SI Appendix*, Eq. **S32** for the Landau Level indexing). The result is shown in Fig. 5*B* for two angles, using the data from Fig. 5*A* (more plots for 12 angles are shown in *SI Appendix*, Fig. S7). At B much larger than $B_0 \approx 20$ T, the indexing plot is quite linear, in agreement with the above-mentioned rough B-periodic pattern. However, as B gets closer to B_0, the curves become nonlinear. The nonlinear dependence of the Landau-Level index as a function of $1/B$ is also displayed in *SI Appendix*, Fig. S5*D*; such behavior contrasts sharply with that of conventional quantum oscillations in metals.

Fig. 5*C* displays results from conducting Landau index fitting for all the measured tilt angles using *SI Appendix*, Eqs. **S32** and **S34**. The procedure to obtain ΔB and the corresponding uncertainty are discussed in *SI Appendix*, section S4. The obtained ΔB values from $\frac{\mathrm{d}\tau}{\mathrm{d}H}$ (red dots) and ${\frac{\mathrm{d}^2\tau}{\mathrm{d}H}}^2$ (blue dots) are consistent with each other. Notably, ΔB shows a large change which follows closely the $\cos(\theta)$ dependence predicted by Eq. **4**. This is a strong indication that the oscillations depend on the c-component of the magnetic field and that they have an orbital origin.

We have fitted the temperature-dependent data using the standard 2D LK form for a parabolic band with mass m^*. The Dirac spectrum requires a different expression for a (60, 61). However, it can be cast in terms of m^*/m_e with the following relation:

$$\frac{m^*}{m_e} = \frac{(g'/2)\mu_B(B - B_0)}{|\alpha|v_D^2 m_e}. \qquad \textbf{[5]}$$

Note that $\frac{m^*}{m_e}$ is independent of the angle θ and proportional to $B - B_0$. In Fig. 3*C* we find an average value of $\frac{m^*}{m_e} \approx 4$. The prediction that m^* increases with increasing B as $B - B_0$ is also in rough agreement with the LK fit of the amplitude at fixed B shown in *SI Appendix*, Fig. S5*C*. We note that Eqs. **4** and **5**, depend on a single unknown parameter $|\alpha|v_D^2$. Using the measured value of ΔB, We can use Eq. **4** to extract the product $\sqrt{|\alpha|}v_\mathrm{D}$. Taking

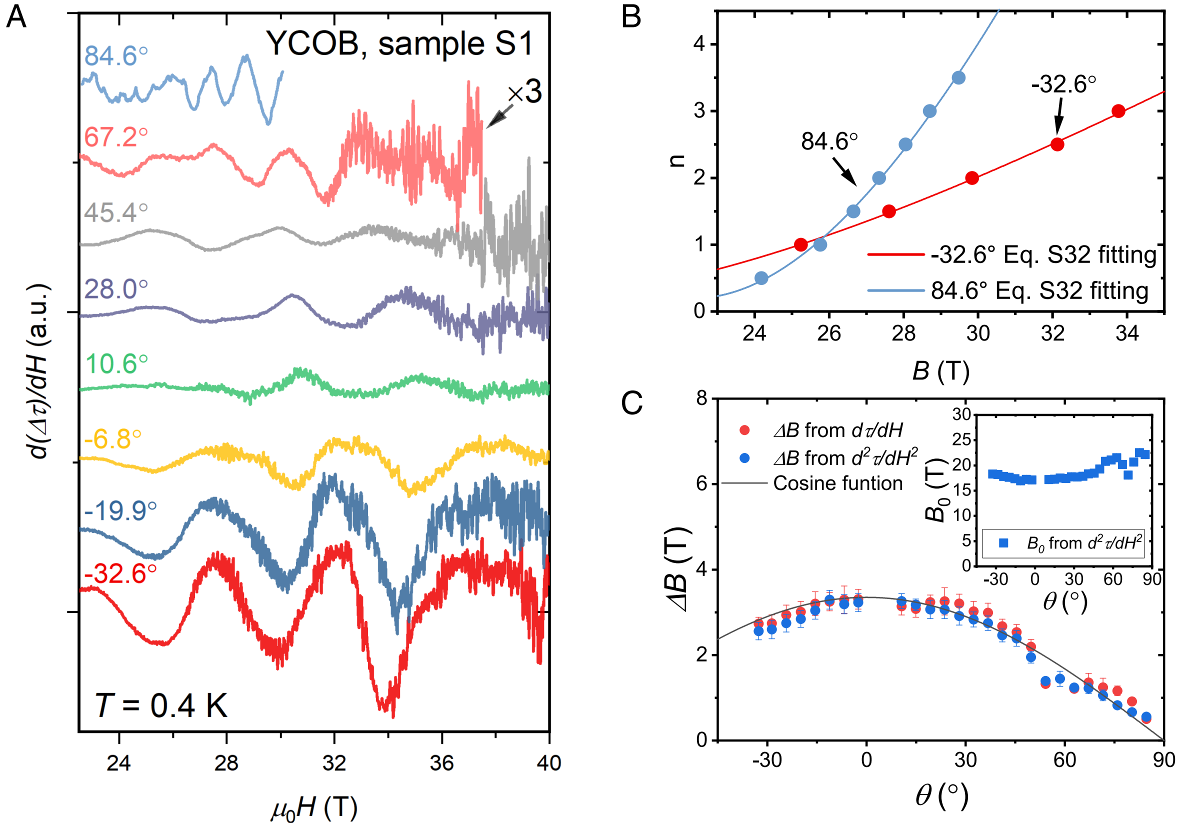

Fig. 5. Angular dependence of the magnetic oscillations. (*A*) The oscillations in dτ/dH at different angles. The oscillation component was obtained after subtraction of a Loess-smoothed background. The background subtraction method is shown in *SI Appendix*, Fig. S5*A*. "×3" means the amplitudes are multiplied by 3 for clarity. (*B*) Landau index plot of the oscillations at $\theta = -32.6°$ and 84.6° in (*A*). maximum and minimum of the oscillations are taken to be integer and half-integer values n and $n + 1/2$. Solid curves show the fitting results of the function $n = (B - B_0)^2/(\Delta B \cdot B) - (\varphi + \pi)/2\pi$ based on *SI Appendix*, Eq. **S32**. (*C*) The period of oscillation ΔB versus angle θ. ΔB was obtained from fitting of the Landau index plots of both dτ/dH (red dots) and d$^2\tau$/dH^2 (blue dots) at different angles. The procedure is described in *SI Appendix*, section S4 and data for 12 angles are shown in *SI Appendix*, Fig. S7. Following Eq. **4** a cosine fit for ΔB versus θ is shown in the black curve. *Inset*: The parameter B_0 versus angle θ from the fitting of d$^2\tau$/dH^2 data in *SI Appendix*, Fig. S7.

$g' = 2g \approx 4$ we find $\sqrt{|\alpha|}v_{\mathrm{D}} \approx 39$ meV·Å$\approx 5.89 \times 10^3$ m/s. Plugging this into Eq. **5** and using $B - B_0 = 10$ T, we find $m^*/m = 5.78$, in reasonable agreement with the value 4 from the LK fit.

Since m^* is extracted from the temperature dependence and ΔB from the period, the agreement of the value of m^* extracted from two independently measured quantities serves as a stringent test of the model of fermions with Landau level quantization; its validation provides key support for this picture.

Origin of the Gauge Magnetic Field

Now, we address a key question: In the spinon model, what is the origin of the gauge magnetic field b, and how is it related to the applied field? The literature has discussed two possibilities. This discussion is quite general and applies equally well to spinon with any dispersion, whether it is Dirac or not.

1. The spinon–chargon mechanism. Instead of a spin Hamiltonian, we go back to the Hubbard model with finite onsite repulsion U and hopping t, which includes charge fluctuations described by a gapped boson called chargon (62). Even though the spinon is charge neutral, its current is accompanied by a backflow of orbital chargon current, which couples to the external B field. In this way, b is proportional to the c-component of the magnetic field $B\cos(\theta)$ (*SI Appendix*, section S9.) A physical way to view this effect in spin language was given by Motrunich for a triangular lattice (11). He showed that there is a linear coupling between the physical magnetic flux through a triangle on-site i, j, k and the scalar chirality $C = \langle \vec{S}_i \cdot (\vec{S}_j \times \vec{S}_k)\rangle$. Wen, Wilczek, and Zee (63) showed that a spinon hopping around the triangle picks up a Berry phase given by C, which is interpreted as the gauge flux through the triangle. Hence, $b \propto C \propto B\cos(\theta)$. Near the Mott transition, the ratio $\alpha = \frac{b}{B\cos(\theta)}$ is of order unity (11) but is expected to diminish as the Mott band gap increases.
2. The DM mechanism. In a recent paper (64), it is pointed out the DM interaction, which is known to exist in these kagome compounds due to the noncollinear Cu-O-Cu bond (Fig. 1*A*), can give rise to an effective gauge field. The idea is that even in the absence of spin ordering, the DM term causes a canting of the nearest neighbor spins on sites i, j, so that $\langle(\vec{S}_j \times \vec{S}_k)\rangle$ has an average z component. In the presence of spin polarization $\langle \vec{S}_z\rangle$ is also nonzero. As a result, the scalar chirality on three sites that form a triangle $C = \langle \vec{S}_i \cdot (\vec{S}_j \times \vec{S}_k)\rangle$ is finite and $\propto \langle \vec{S}_z\rangle$ after a mean-field factorization. Since b is proportional to the chirality C (63), we write $b = \gamma\langle \vec{S}_z\rangle$, where γ is a constant. Note that b is again proportional to $\cos(\theta)$. In ref. 64, it was shown that this mechanism generates a gauge magnetic field which is equivalent to 120 T in a direction opposed to the external B, hence $\alpha \approx -4$. Note that this description

> deals only with spins and remains valid in a large band gap insulator. Its origin is spin–orbit coupling, which makes the orbital nature of the effect physically more transparent.

In the spinon–chargon mechanism α is a constant but in the DM mechanism, $|\alpha| = \gamma\langle|\vec{S}|\rangle/B$ and can have some B dependence if $|\langle\vec{S}\rangle|$ is not linear in B, as is the case near the $\frac{1}{9}$ plateau. However, this dependence is less than 12% in the relevant B range between 20 T and 40 T, as shown in the *Inset* of *SI Appendix*, Fig. S11*A*. *SI Appendix*, Fig. S11*B* shows the data fitted using the DM mechanism; the fit quality and the resulting parameters are similar to those from the spinon–chargon mechanism. Below, we will continue our discussion assuming a constant α. Recall that we use Eq. **4** to extract $\sqrt{|\alpha|}v_D \approx 39$ meV·Å. The velocity itself can be extracted from the slope of χ versus B, yielding the average of $v_D \approx 29.3\sqrt{M_\downarrow/9}$ meV·Å, where $M_\downarrow$ is the number of Dirac nodes in the original Brillouin zone which is multiple of 3 due to unit cell tripling (*SI Appendix*, section S8). In *SI Appendix*, section S1, we use the linear T term in Fig. 1c *Inset* to extract a very similar value of $v_D \approx 34.1\sqrt{M_\downarrow/9}$ meV·Å. We find that $|\alpha|$ is ≈ 1.33 and 2.3 if $M_\downarrow$ is 9 or 3 respectively. In the DM mechanism, it is estimated that $|\alpha| \approx 4$ (64) while in the spinon–chargon mechanism, $\alpha \approx t/U$, which would be somewhat less than unity (*SI Appendix*, section S9). Thus our analysis tends to favor the DM mechanism.

Summary and Conclusions

In summary, we report the identification of a $\frac{1}{9}$ magnetization plateau in the Mott insulator YCOB under an intense magnetic field. Right above this field, magnetic oscillations appear in the magnetic torque of this robust insulator with a charge gap of 3 eV. The data are well reproduced in several samples (*SI Appendix*, Fig. S10, detailed discussion in *SI Appendix*, section S6). These oscillations are characterized by the following key features. 1) The oscillations are roughly periodic in large applied fields B. 2) Their period, ΔB, follows a $\cos\theta$ dependence, suggesting that they are caused by an orbital effect. 3) The T dependence of the oscillation amplitude is consistent with the LK formula. Point 1) and the fact that the oscillations are tied to the $\frac{1}{9}$ plateau rule out trivial explanations such as small metallic inclusions. Our data do not resemble structures in the magnetization curves that have been reported up to now, which have been interpreted based on conventional pictures of multiple magnetic phase transitions. In contrast, a phenomenological Dirac spinon model based on the spin liquid picture was successful in organizing the complex evolution of the oscillations as a function of field, angle, and temperature.

Materials and Methods

Single crystals of $YCu_3(OH)_6Br_2[Br_{1-y}(OH)_y]$ (YCOB) were grown using the hydrothermal method and ultrasonically cleaned in water before measurements to remove the possible impurities as reported previously (22, 34). The deuterated single crystals (YCOB-D, samples D1 and D2) were synthesized using the same method with the corresponding deuterated starting materials and heavy water. The OH content of these samples (S1, S2, S5, M1, and M2) is given by $y = 0.67$. The Cl-doped single crystals (YCOB-58%Cl) were synthesized using the same method as YCOB with 58% of the Br atoms replaced by Cl atoms, and y is estimated to be 0.03. These values have been determined by single crystal X-ray diffraction. YCOB samples S1, S2, S5, and M1 come from the same growth batch, while sample M2 comes from another batch. The measurement conditions and observations of all samples are listed in *SI Appendix*, Table S1.

Magnetization measurements at low field (<14 T) were carried out in a Quantum Design physical property measurement system (PPMS Dynacool-14T) using the Vibrating Sample Magnetometer option.

Magnetization measurements on YCOB M1 and M2 at high field were using a compensated-coil spectrometer (33, 65) as drawn in the *Inset* of *SI Appendix*, Fig. S2*A* which were performed at 65 T and 73 T pulsed field magnet at the National High Magnetic Field Laboratory (NHMFL), Los Alamos. YCOB M1 was stacked in a Vespel ampoule with *c*-axis aligned first and then restacked with *ab*-plane aligned to apply the magnetic field in the *ab*-plane.

Magnetic torque measurements on YCOB S1, S2, and YCOB-D D1 were using a piezo-resistive cantilever as drawn in Fig. 2*A* performed in 41 T Cell 6 (YCOB S1 and YCOB-D D1) and 45 T Hybrid (YCOB S2) DC field magnets in NHMFL, Tallahassee. The unloaded cantilever setup signals are measured in PPMS as shown in *SI Appendix*, Fig. S1*A*. The angles of YCOB S1 measured in Cell 6 are adjusted by comparing the signal measured in PPMS under the same condition as shown in *SI Appendix*, Fig. S1*B*. Note that the torque signals have larger positive peaks, which is caused by the asymmetric response of the piezo-cantilever to tension and compression. This has an effect on the quantum oscillation amplitude as a function of angle but will not affect the analysis of the period or the temperature dependence at fixed angle.

Magnetic torque measurements on YCOB S5 were using a piezo-resistive cantilever performed in the 55 T Mid-Pulse magnet in NHMFL, Los Alamos.

Magnetic torque measurements on YCOB-D D2 were using a capacitive cantilever performed in 41 T Cell 6 DC field magnets in NHMFL, Tallahassee.

The expression of Landau index fitting in Fig. 5*B* is *SI Appendix*, Eq. **S32**: $n = (B - B_0)^2/(\Delta B \cdot B) - (\varphi + \pi)/2\pi$, where $B_0 = 17.78$ T, $\Delta B = 2.74$ T, and $\varphi = -1.4\pi$ for -32.6°; while $B_0 = 22.40$ T, $\Delta B = 0.50$ T, and $\varphi = -1.4\pi$ for 84.6°.

The expression of cosine fitting in Fig. 5*C* is $\Delta B(\theta) = \Delta B(0)\cos\theta$, and the fitted result is $\Delta B(0) = 3.35$ T.

Data, Materials, and Software Availability. The data generated in this study have been deposited in the OSF repository (66). All other data are included in the article and/or *SI Appendix*.

ACKNOWLEDGMENTS. The work at the University of Michigan is supported by the Department of Energy under Award No. DE-SC0020184 (magnetization measurements) to G.Z., Y.Z., K.-W.C., K.J., A.C., and L.L. A portion of this work was performed at the National High Magnetic Field Laboratory (NHMFL), which is supported by NSF Cooperative Agreement Nos. DMR-1644779 and DMR-2128556 and the Department of Energy (DOE). J.S. acknowledges support from the DOE BES program "Science at 100 T," which permitted the design and construction of much of the specialized equipment used in the high-field studies. The Institute of Physics China provided in 2023 the crystals U-M used to generate data for this project. The crystal growth work at and by the Institute of Physics China was supported by the National Key Research and Development Program of China (Grants 2022YFA1403400, No. 2021YFA1400401), the K. C. Wong Education Foundation (Grants No. GJTD-2020-01), and the Strategic Priority Research Program (B) of the Chinese Academy of Sciences (Grants No. XDB33000000). The experiment in NHMFL is funded in part by a QuantEmX grant from Institute for Complex Adaptive Matter and the Gordon and Betty Moore Foundation through Grant No. GBMF5305 to G.Z., Y.Z., K.-W.C., D.Z., K.J., and A.C. P.A.L. acknowledges the support by DOE office of Basic Sciences Grant No. DE-FG02-03ER46076 (theory).

Author affiliations: [a]Department of Physics, University of Michigan, Ann Arbor, MI 48109; [b]Department of Physics, Massachusetts Institute of Technology, Cambridge, MA 02139; [c]Beijing National Laboratory for Condensed Matter Physics, Institute of Physics, Chinese Academy of Sciences, Beijing 100190, China; [d]School of Physical Sciences, University of Chinese Academy of Sciences, Beijing 100190, China; [e]National High Magnetic Field Laboratory, MS E536, Los Alamos National Laboratory, Los Alamos, NM 87545; and [f]Songshan Lake Materials Laboratory, Dongguan, Guangdong 523808, China

1. Z. Xiang *et al*., Quantum oscillations of electrical resistivity in an insulator. *Science* **362**, 65–69 (2018).
2. L. Li, K. Sun, C. Kurdak, J. Allen, Emergent mystery in the Kondo insulator samarium hexaboride. *Nat. Rev. Phys.* **2**, 463–479 (2020).
3. B. Tan *et al*., Unconventional fermi surface in an insulating state. *Science* **349**, 287–290 (2015).
4. Z. Xiang *et al*., Unusual high-field metal in a Kondo insulator. *Nat. Phys.* **17**, 788–793 (2021).
5. D. Chowdhury, I. Sodemann, T. Senthil, Mixed-valence insulators with neutral fermi surfaces. *Nat. Commun.* **9**, 1766 (2018).
6. I. Sodemann, D. Chowdhury, T. Senthil, Quantum oscillations in insulators with neutral fermi surfaces. *Phys. Rev. B* **97**, 045152 (2018).
7. P. W. Anderson, Resonating valence bonds: A new kind of insulator? *Mater. Res. Bull.* **8**, 153–160 (1973).
8. P. W. Anderson, The resonating valence bond state in La_2CuO_4 and superconductivity. *Science* **235**, 1196–1198 (1987).
9. L. Savary, L. Balents, Quantum spin liquids: A review. *Rep. Prog. Phys.* **80**, 016502 (2016).
10. Y. Zhou, K. Kanoda, T. K. Ng, Quantum spin liquid states. *Rev. Mod. Phys.* **89**, 025003 (2017).
11. O. I. Motrunich, Orbital magnetic field effects in spin liquid with spinon Fermi sea: Possible application to κ-$(ET)_2Cu_2(CN)_3$. *Phys. Rev. B* **73**, 155115 (2006).
12. Y. Ran, M. Hermele, P. A. Lee, X. G. Wen, Projected-wave-function study of the spin-1/2 Heisenberg model on the Kagomé lattice. *Phys. Rev. Lett.* **98**, 117205 (2007).
13. M. Hermele, Y. Ran, P. A. Lee, X. G. Wen, Properties of an algebraic spin liquid on the Kagome lattice. *Phys. Rev. B* **77**, 224413 (2008).
14. M. Norman, Colloquium: Herbertsmithite and the search for the quantum spin liquid. *Rev. Mod. Phys.* **88**, 041002 (2016).
15. T. H. Han *et al*., Fractionalized excitations in the spin-liquid state of a Kagome-lattice antiferromagnet. *Nature* **492**, 406–410 (2012).
16. R. W. Smaha *et al*., Site-specific structure at multiple length scales in Kagome quantum spin liquid candidates. *Phys. Rev. Mater.* **4**, 124406 (2020).
17. D. E. Freedman *et al*., Site specific X-ray anomalous dispersion of the geometrically frustrated Kagomé magnet, Herbertsmithite, $ZnCu_3(OH)_6Cl_2$. *J. Am. Chem. Soc.* **132**, 16185–16190 (2010).
18. M. A. de Vries, K. V. Kamenev, W. Kockelmann, J. Sanchez-Benitez, A. Harrison, Magnetic ground state of an experimental $s = 1/2$ Kagome antiferromagnet. *Phys. Rev. Lett.* **100**, 157205 (2008).
19. Y. Wei *et al*., Nonlocal effects of low-energy excitations in quantum-spin-liquid candidate $Cu_3Zn(OH)_6FBr$. *Chin. Phys. Lett.* **38**, 097501 (2021).
20. T. Asaba *et al*., High-field magnetic ground state in $s = 1\ 2$ Kagome lattice antiferromagnet $ZnCu_3(OH)_6Cl_2$. *Phys. Rev. B* **90**, 064417 (2014).
21. X. H. Chen, Y. X. Huang, Y. Pan, J. X. Mi, Quantum spin liquid candidate $YCu_3(OH)_6Br_2[Br\,(OH)_{1-}]$ (x *approx* 0.51): With an almost perfect Kagomé layer. *J. Magn. Magn. Mater.* **512**, 167066 (2020).
22. Z. Zeng *et al*., Possible Dirac quantum spin liquid in the Kagome quantum antiferromagnet $YCu_3(OH)_6Br_2[Br_x(OH)_{1-x}]$. *Phys. Rev. B* **105**, L121109 (2022).
23. J. Liu *et al*., Gapless spin liquid behavior in a Kagome Heisenberg antiferromagnet with randomly distributed hexagons of alternate bonds. *Phys. Rev. B* **105**, 024418 (2022).
24. X. Hong *et al*., Heat transport of the Kagome Heisenberg quantum spin liquid candidate $YCu_3(OH)_{6.5}Br_{2.5}$: Localized magnetic excitations and a putative spin gap. *Phys. Rev. B* **106**, L220406 (2022).
25. W. Sun, Y. X. Huang, S. Nokhrin, Y. Pan, J. X. Mi, Perfect kagomé lattices in $YCu_3(OH)_6Cl_3$: A new candidate for the quantum spin liquid state. *J. Mater. Chem. C* **4**, 8772–8777 (2016).
26. A. Zorko *et al*., Coexistence of magnetic order and persistent spin dynamics in a quantum Kagome antiferromagnet with no intersite mixing. *Phys. Rev. B* **99**, 214441 (2019).
27. O. Cépas, C. M. Fong, P. W. Leung, C. Lhuillier, Quantum phase transition induced by Dzyaloshinskii-Moriya interactions in the Kagome antiferromagnet. *Phys. Rev. B* **78**, 140405 (2008).
28. B. Bernu, L. Pierre, K. Essafi, L. Messio, Effect of perturbations on the kagome $s = \frac{1}{2}$ antiferromagnet at all temperatures. *Phys. Rev. B* **101**, 140403 (2020).
29. L. Messio, O. Cépas, C. Lhuillier, Schwinger-boson approach to the kagome antiferromagnet with Dzyaloshinskii-Moriya interactions: Phase diagram and dynamical structure factors. *Phys. Rev. B* **81**, 064428 (2010).
30. D. Chatterjee *et al*., From spin liquid to magnetic ordering in the anisotropic Kagome y-kapellasite $Y_3Cu_9(OH)_{19}Cl_8$: A single-crystal study. *Phys. Rev. B* **107**, 125156 (2023).
31. A. Xu *et al*., Magnetic ground states in the Kagome system $YCu_3(OH)_6\ [(Cl_xBr_{1-x})_3$-y(OH) y]. *Phys. Rev. B* **110**, 085146 (2024).
32. Z. Zeng *et al*., Spectral evidence for Dirac spinons in a Kagome lattice antiferromagnet. *Nat. Phys.* **20**, 1–6 (2024).
33. P. Goddard *et al*., Experimentally determining the exchange parameters of quasi-two-dimensional Heisenberg magnets. *New J. Phys.* **10**, 083025 (2008).
34. J. Schulenburg, A. Honecker, J. Schnack, J. Richter, H. J. Schmidt, Macroscopic magnetization jumps due to independent magnons in frustrated quantum spin lattices. *Phys. Rev. Lett.* **88**, 167207 (2002).
35. Y. Okamoto *et al*., Magnetization plateaus of the spin-1/2 Kagome antiferromagnets volborthite and vesignieite. *Phys. Rev. B* **83**, 180407 (2011).
36. S. Nishimoto, N. Shibata, C. Hotta, Controlling frustrated liquids and solids with an applied field in a Kagome Heisenberg antiferromagnet. *Nat. Commun.* **4**, 2287 (2013).
37. H. Ishikawa *et al*., One-third magnetization plateau with a preceding novel phase in volborthite. *Phys. Rev. Lett.* **114**, 227202 (2015).
38. H. K. Yoshida, Frustrated kagome antiferromagnets under high magnetic fields. *J. Phys. Soc. Jpn.* **91**, 101003 (2022).
39. S. Jeon *et al*., One-ninth magnetization plateau stabilized by spin entanglement in a Kagome antiferromagnet. *Nat. Phys.* **20**, 435–441 (2024).
40. S. Suetsugu *et al*., Emergent spin-gapped magnetization plateaus in a spin-1/2 perfect Kagome antiferromagnet. *Phys. Rev. Lett.* **132**, 226701 (2024).
41. M. Oshikawa, M. Yamanaka, I. Affleck, Magnetization plateaus in spin chains: "Haldane gap" for half-integer spins. *Phys. Rev. Lett.* **78**, 1984 (1997).
42. T. Picot, M. Ziegler, R. Orús, D. Poilblanc, Spin-s kagome quantum antiferromagnets in a field with tensor networks. *Phys. Rev. B* **93**, 060407 (2016).
43. D. Fang, N. Xi, S. J. Ran, G. Su, Nature of the 1/9-magnetization plateau in the spin-1/2 Kagome Heisenberg antiferromagnet. *Phys. Rev. B* **107**, L220401 (2023).
44. L. W. He, S. L. Yu, J. X. Li, Variational monte Carlo study of the 1/9-magnetization plateau in Kagome antiferromagnets. *Phys. Rev. Lett.* **133**, 096501 (2024).
45. J. Sheng *et al*., Two-dimensional quantum universality in the spin-1/2 triangular-lattice quantum antiferromagnet $Na_2BaCo(PO_4)_2$. *Proc. Natl. Acad. Sci. U.S.A.* **119**, e2211193119 (2022).
46. G. Koutroulakis *et al*., Quantum phase diagram of the $s = 1/2$ triangular-lattice antiferromagnet $Ba_3CoSb_2O_9$. *Phys. Rev. B* **91**, 024410 (2015).
47. D. Shoenberg, *Magnetic Oscillations in Metals* (Cambridge University Press, 1984).
48. P. Czajka *et al*., Oscillations of the thermal conductivity in the spin-liquid state of α-$RuCl_3$. *Nat. Phys.* **17**, 915–919 (2021).
49. J. Bruin *et al*., Origin of oscillatory structures in the magnetothermal conductivity of the putative Kitaev magnet α-$RuCl_3$. *APL Mater.* **10**, 090703 (2022).
50. É. Lefrançois *et al*., Oscillations in the magnetothermal conductivity of α-$RuCl_3$: Evidence of transition anomalies. *Phys. Rev. B* **107**, 064408 (2023).
51. S. Suetsugu *et al*., Evidence for a phase transition in the quantum spin liquid state of a kitaev candidate α-$RuCl_3$. *J. Phys. Soc. Jpn.* **91**, 124703 (2022).
52. R. Okuma *et al*., A series of magnon crystals appearing under ultrahigh magnetic fields in a Kagomé antiferromagnet. *Nat. Commun.* **10**, 1229 (2019).
53. K. Zhao *et al*., Realization of the Kagome spin ice state in a frustrated intermetallic compound. *Science* **367**, 1218–1223 (2020).
54. J. Hwang *et al*., Successive magnetic phase transitions and multiferroicity in the spin-one triangular-lattice antiferromagnet $Ba_3NiNb_2O_9$. *Phys. Rev. Lett.* **109**, 257205 (2012).
55. J. Wu *et al*., Magnetic field effects on the quantum spin liquid behaviors of $NaYbS_2$. *Quantum Front.* **1**, 13 (2022).
56. X. Rao *et al*., Survival of itinerant excitations and quantum spin state transitions in $YbMgGaO_4$ with chemical disorder. *Nat. Commun.* **12**, 4949 (2021).
57. Y. Tokiwa *et al*., Magnetic phase transitions in the two-dimensional frustrated quantum antiferromagnet Cs_2CuCl_4. *Phys. Rev. B* **73**, 134414 (2006).
58. N. A. Fortune *et al*., Cascade of magnetic-field-induced quantum phase transitions in a spin-1/2 triangular-lattice antiferromagnet. *Phys. Rev. Lett.* **102**, 257201 (2009).
59. A. Smirnov *et al*., Order by quenched disorder in the model triangular antiferromagnet $RbFe(MoO_4)_2$. *Phys. Rev. Lett.* **119**, 047204 (2017).
60. I. A. Luk'yanchuk, De Haas-van Alphen effect in 2D systems: Application to mono-and bilayer graphene. *Low Temp. Phys.* **37**, 45–48 (2011).
61. CS Küppersbusch, "Magnetic oscillations in two-dimensional Dirac systems and shear viscosity and spin diffusion in a two-dimensional Fermi gas," PhD thesis, Universität zu Köln (2015).
62. S. S. Lee, P. A. Lee, U (1) gauge theory of the hubbard model: Spin liquid states and possible application to κ-$(BEDT$-$TTF)_2Cu_2(CN)_3$. *Phys. Rev. Lett.* **95**, 036403 (2005).
63. X. G. Wen, F. Wilczek, A. Zee, Chiral spin states and superconductivity. *Phys. Rev. B* **39**, 11413 (1989).
64. B. Kang, P. A. Lee, Generation of gauge magnetic fields in a kagome spin liquid candidate using the Dzyaloshinskii-Moriya interaction. *Phys. Rev. B* **109**, L201104 (2024).
65. P. Goddard *et al*., Separation of energy scales in the kagome antiferromagnet TmAgGe: A magnetic-field-orientation study up to 55 T. *Phys. Rev. B* **75**, 094426 (2007).
66. G. Zheng, Unconventional magnetic oscillations in a kagome mott insulator. OSF. https://osf.io/jstex/. Deposited 11 January 2025.